

Article

Applied Magnetic Field Increases Magnetic Anisotropy in HDDR-Processed Nd-Fe-B Alloy

Zachary P. Tener ¹, Xubo Liu ², Ikenna C. Nlebedim ², Matthew J. Kramer ², Michael A. McGuire ¹
and Michael S. Kesler ^{1,*}

¹ Oak Ridge National Laboratory, Oak Ridge, TN 37830, USA; zachary.tener@sml.doe.gov (Z.P.T.)

² Ames National Laboratory, Ames, IA 50011, USA

* Correspondence: keslerms@ornl.gov

Abstract: We investigate the effect of an applied magnetic field on the entire HDDR process using a customized reactor vessel and a warm-bore superconducting magnet. We analyzed the resulting properties produced at both a 0 applied field and a 2 Tesla applied field. We show that the application of a magnetic field throughout the HDDR process results in powders that exhibit a greater level of anisotropy compared to their ambient field counterparts.

Keywords: X-ray diffraction; SQUID magnetometry; hydrogenation; remanence; coercivity; degree of alignment

1. Introduction

As the development of modern technology demands magnets of greater energy products, so too does the economic and environmental cost of the current state-of-the-art magnets based on the Nd₂Fe₁₄B structure increase. These magnets have two industrially viable forms, the “sintered” and “bonded” varieties. Sintered magnets are manufactured using a very specific, often proprietary process where the cast magnetic material is pulverized, milled to a small size, aligned in a magnetic field, and then “sintered,” or by heating the powdered material such that it fuses into a bulk solid. Post-processing, machining, and coating are then performed before magnetizing the material. Bonded magnets also use pulverized feedstock, but rather than sintering, the powder is mixed and cast in a resin or polymer. Of the two, sintered magnets currently hold the record for many of the relevant magnetic properties, including magnetic saturation, coercivity, maximum energy product, and anisotropy [1,2].

Bonded magnets, on the other hand, have the advantage of being produced in near-net-shape geometry, and they possess high resistivity, which suppresses internal eddy currents. One method to produce the anisotropic nanocrystalline powder necessary for a bonded magnet with greater magnetic properties [3] is to use a hydrogen treatment. The hydrogen treatment has decades of research and optimization toward improving the powder’s resultant magnetic properties, beginning with the first report of the process in 1989 [4,5] and its formalized naming in 1991 [6]. Despite the performance advancements of sintered magnets, the economic and environmental impact of the two options (in both initial feedstock, processing, and material lifetime) are not directly correlated to that performance and require consideration prior to technological application.

The current nomenclature for these treatments represents two different procedures: hydrogen decrepitation (denoted HD* in this paper) and hydrogenation–disproportionation–desorption–recombination (HDDR) [6–9]. HD* utilizes an ambient to low-temperature treatment in a hydrogen environment. This causes the hydrogen to intercalate into the grain boundaries of the material. The resulting expansion of the unit cells in the grain boundary phases causes them to “crack,” reducing the particle size of the Nd-Fe-B feedstock [10].



Citation: Tener, Z.P.; Liu, X.; Nlebedim, I.C.; Kramer, M.J.; McGuire, M.A.; Kesler, M.S. Applied Magnetic Field Increases Magnetic Anisotropy in HDDR-Processed Nd-Fe-B Alloy. *Metals* **2024**, *14*, 294. <https://doi.org/10.3390/met14030294>

Academic Editors: Victorino Franco, João Horta Belo and Luis Miguel Moreno-Ramírez

Received: 2 January 2024
Revised: 22 February 2024
Accepted: 26 February 2024
Published: 1 March 2024



Copyright: © 2024 by the authors. Licensee MDPI, Basel, Switzerland. This article is an open access article distributed under the terms and conditions of the Creative Commons Attribution (CC BY) license (<https://creativecommons.org/licenses/by/4.0/>).

The result of this process is a relatively fine powder consistent with the grain size of the preceding microstructure.

HDDR, on the other hand, is a high-temperature process ($>630\text{ }^{\circ}\text{C}$) that consists of two distinguishable steps, the “HD” step and the “DR” step. In the HD step, the material of interest (typically a rare-earth, transition metal intermetallic) is subjected to a targeted high temperature in a reducing environment containing hydrogen. The hydrogen intercalates into the material (“hydrogenation”) and then reacts with the rare earth in the rare-earth magnet phase and rare-earth rich-grain boundary phases, resulting in hydrides and other binary and elemental products (“disproportionation”). This has a simultaneous volumetric effect on the unit cells of the phases involved [10] such that the average grain size is reduced significantly compared to the original state.

After a specified dwell time, the DR step is performed either at the same or different temperature as the HD step, or the temperature can be altered. The hydrogen environment is removed via either a vacuum or flushing with a noble gas (“desorption”), and the temperature is held, causing the “recombination” of the material into its parent phase. The kinetics of the recombination are found to be of extreme importance to the final microstructure and its magnetic properties. This process requires optimizing many parameters and the composition dependence of those parameters. Some of the work discussing the optimization of some processing parameters is summarized in Table 1.

Table 1. Most relevant parameters considered in an HDDR process. The references are to works that specifically study controlled variation of those parameters. Some unique processes contain even more variables. It should be noted that compositional studies are not included in this table but are of the utmost importance in the optimization process.

HDDR Step	Thermal Processing Parameters	Pressure Processing Parameters
HD *	Temp. Ramp Rate [11]	H ₂ % in Supply Gas * [10–18]
	Dwell Temp. [19–24]	Total Pressure * [25]
	Dwell Time [10,21,24,26,27]	Gas Introduction Temp. [11,22,23,26]
DR	Temp. Ramp Rate [none]	1st Vacuum Pressure [28,29]
	Dwell Temp. [19,22,23,30–32]	2nd Vacuum Pressure [33]
	Dwell Time [16,26,28,29,31,32,34,35]	-
	Cooling Rate [none]	-

* In much of the literature, the hydrogen partial pressure is given as the processing parameter, and the total pressure of the supplied gas may not be formally addressed.

When HDDR is performed on Nd-Fe-B feedstock, there is a significant difference in the magnetic properties of the parent compound and the HD products, namely NdH_{2.4-x}, Fe, and Fe₂B. To utilize this difference for optimization, in 1996, the use of a magnetic field was introduced as an additional processing parameter [36]. Liesert et al. reported the application of a 7 T magnetic field, if utilized during the entirety of the HDDR process, yielded magnetically isotropic powders. However, it was noted that when the field was only applied to Nd₂Fe₁₄B crystallites (presumably formed during the desorption and recombination step) the result was an anisotropic powder when magnetization measurements were performed in parallel and perpendicular orientations relative to the alignment field. The magnetization measured parallel to the applied field resulted in magnetic property values of $M_R \approx 88\text{ emu/g}$, $H_c \approx 2.76\text{ kOe}$, and $BH_{\max} \approx 5.2\text{ MGOe}$ (values estimated using a digitized image).

That same year, Courtois et al. investigated the effect of an applied magnetic field on Nd-Fe-B crystallites in a Nd/Cu eutectic matrix and found they could optimize the magnetic response by liquifying the eutectic, orienting the particles, and resolidifying the eutectic, as long as they did not go over a critical temperature of $1100\text{ }^{\circ}\text{C}$, whereafter

they lost the ability to orient and observe a decrease in the alignment via magnetization measurements [37].

This methodology of utilizing a Nd/Cu eutectic under an applied field was explored by Liesert in 1997 [32]. They found that without the eutectic, their HDDR process resulted in magnetically isotropic powder under a 7 T applied field. However, with their eutectic, they found that at a recombination dwell time of 6 h, their powders had a high coercivity and anisotropy. At a dwell time of 10 h, the powders had a similar degree of anisotropy, but their coercivity had decreased, and their magnetic remanence value had increased. Rivoirard performed a similar experiment using Nd-Fe-B alloy ribbon in a Nd/Cu eutectic, but at a 16 T field and without any hydrogen involved in the processing [38]. They found that the texture ratio of their material increased linearly with an applied field at 0 T, 4 T, 7 T, and 16 T.

A continuous magnetic field during HDDR was tangentially explored by de Rango et al. when they performed thermomagnetic measurements at 2 kOe (0.2 T) throughout the HDDR process; however, the effect of the field compared to the ambient conditions was not explored [39]. In 2009–2010, Luo et al. investigated the effect of 0, 1, 3, and 5 T of applied magnetic field during a continuous HDDR process followed by an annealing step with no field, concluding that the greatest combination of magnetic properties occurred with the 3 T applied field [40,41]. However, details regarding their unique HDDR processing parameters are left out of the text (mainly related to pressure during their DR step), making this result difficult to replicate.

Finally, work has been performed using HDDR on Sm-Co systems with an applied field during the recombination step [42,43]. It was shown that due to the difference in the magnetic contribution to the Gibbs Free Energy of the Sm-Co phase compared to elemental Co, the recombination reaction was pushed to higher temperatures as the applied field was increased from 0.2 T to 2.3 T to 4.1 T. Though the phase stability with temperature in hydrogen varies considerably between the Sm-Co and Nd-Fe-B systems, this magnetization difference between parent and child phases behaves similarly, as the magnetic transition metal elements resulting from HD have greater magnetic saturation values than the parent rare-earth magnet phase.

These works inspired our use of an applied magnetic field throughout the HDDR process. The field is expected to have a myriad of non-trivial effects, ranging from gas-solid reactivity to reduced microstructural grain size to thermodynamic stabilization and destabilization of para- and ferro-magnetic phases. In addition, the effect of magnetic field annealing is expected to promote directional ordering through the alignment of the final product (the Nd-Fe-B ternary phase) due to the material's structural and magnetic anisotropy. The super-structural ordering of the material may be influenced by local atomic ordering changes induced by the external magnetic field. The culmination of each of these effects is difficult to predict, but their combined influence on the resultant properties of the material may result in interesting observable phenomena.

In this work, we have developed a unique dynamic-HDDR methodology that utilizes a magnetic field throughout the sequential HD and DR steps on a ternary Nd-Fe-B composition. We show how the application of a 2 Tesla field results in material that consistently has a higher anisotropy relative to the samples processed at an ambient field with all other parameters held constant.

2. Materials and Methods

Alloys with nominal composition of Nd₁₄Fe₈₁B₇ were arc-melted and drop-cast into a cylinder-shaped ingot with a diameter of 12 mm. The sample was annealed in an inert environment (sealed in a quartz tube under an Ar pressure of ¼ atm) at 1293 K for 120 h. Powder X-ray diffraction (Panalytical, Worcestershire, UK) of two different sections shows only peaks of Nd₂Fe₁₄B in one section, and the presence of α -Fe and *fcc*-NdO_x in the other, indicating that the casting method performed resulted in an inhomogeneous feedstock.

The reaction chamber setup used here is illustrated in Figure 1. Prior to processing, the surface layer was ground away with a belt sander and sectioned using a low-speed diamond saw into 1 mm thick, 10 mm diameter discs. These discs were ground with fine-grit sandpaper, cleaned with absolute ethanol, broken in half into semicircle shapes, wrapped in tantalum foil, and placed at the end of an alumina boat. Zr foil was added to the boat as an oxygen getter, and a thermocouple was attached to the boat with 90% nickel, 10% chromium alloy wire as close to the sample as possible without contact.

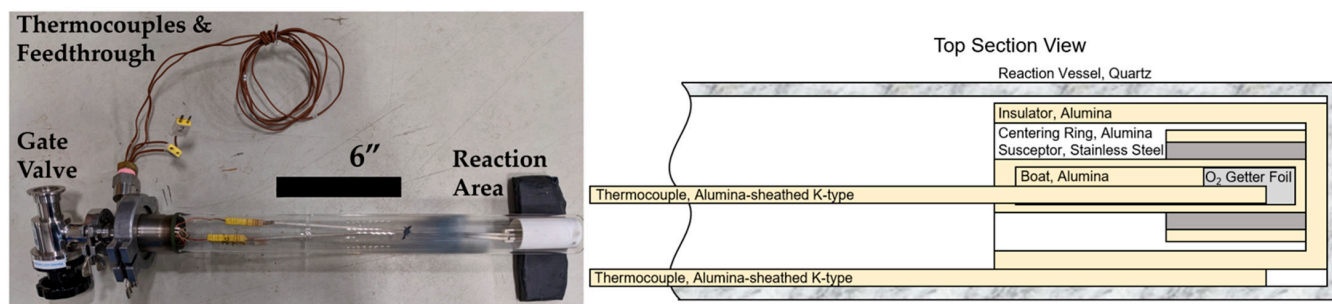


Figure 1. The custom HDDR reaction vessel with key areas labeled (left). The materials used in the reaction area are shown schematically on the (right). The sample is located inside the O₂ getter foil.

The alumina boat was placed such that the sample was concentric within a stainless steel susceptor (the susceptor rather than the sample itself is heated by the induction coil). The susceptor was insulated radially from the reaction vessel quartz via a slightly larger diameter alumina tube acting as a centering ring, followed by a larger alumina crucible insulator. An additional thermocouple was loaded to measure the temperature on the outside of this insulating alumina (See Figure 1) to prevent possible temperature runaway and experiment failure.

This arrangement was loaded into the custom-built reaction vessel consisting of a 2-inch diameter quartz tube sealed to a quick-fit flange. This flange was sealed to a commercially available elbow valve with vacuum-tight feedthroughs for thermocouple connections (see Figure 1). The entirety of the reaction vessel rested within the inner bore of an insert containing a copper induction coil, which itself was centered within the bore of an American Magnetics 9 Tesla superconducting magnet. This allowed for material processing from ambient conditions to applied fields up to 9 T.

The processing procedure followed a “dynamic” HDDR methodology (“dynamic” indicates the gas was slowly removed during the DR step), and the heating profile is shown in Figure 2. The sample underwent the hydrogenation–disproportionation (HD) step, which consisted of evacuating the reaction vessel to ~10 mTorr and then introducing the hydrogen supply gas at an overpressure connected to an oil bubbler (flow rate is approximately 0.5 cc/s). Based on previous literature, a supply gas consisting of 30% H₂ balanced with Ar was utilized [18]. The stainless steel susceptor was directly induction-heated with the induction coil, and the sample within was consequently heated with the stainless steel susceptor via convection and/or radiative heating. Samples were heated in the presence of the hydrogen supply gas at 50 °C/min to 760 °C, where they were held for an hour. The temperature ramp rate is such that the sample is not entirely decrepitated prior to disproportionation, as evidenced by its morphology after the HDDR process is complete. The sample morphology (post-HDDR) generally looks as if the initial semicircle-shaped sample has been broken into three or four large fractions, each of which can be easily ground into powder with mortar and pestle.

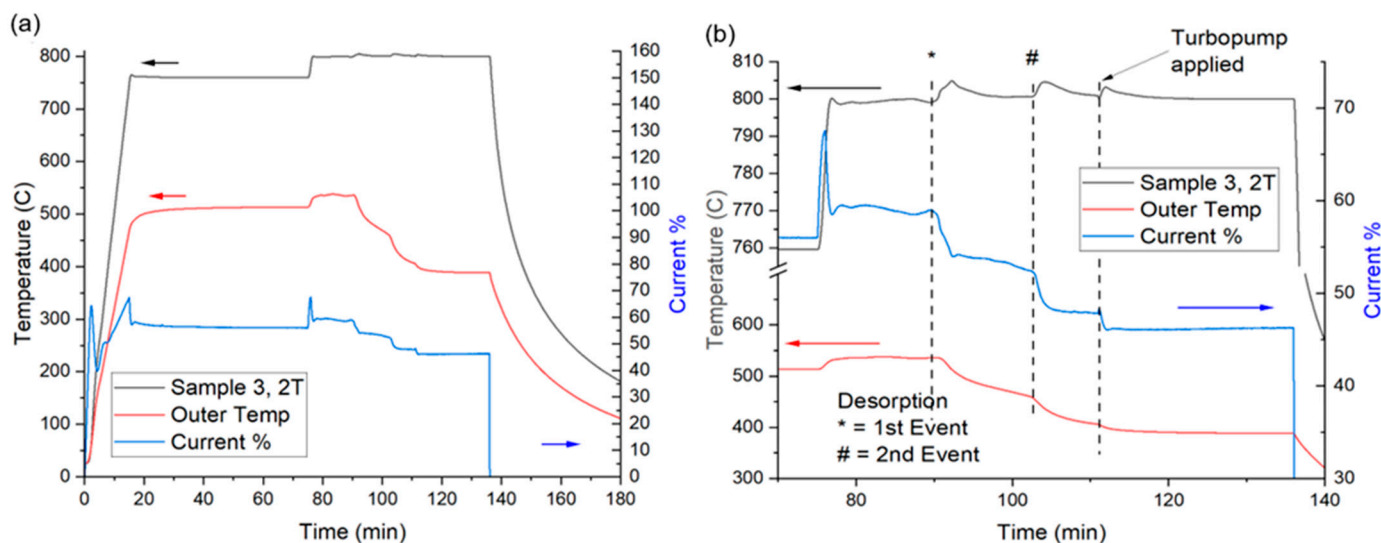


Figure 2. (a) The full heating profile for sample 3 is shown. These temperature profiles are the measured temperatures rather than setpoint. A noticeable feature can be seen at approx. 75 min, indicating the start of the DR step and the 40 °C temperature ramp. (b) is the magnified profile for the DR step. A spike in the measured sample temperature represents the completion of a desorption event (indicated with *). This is followed by a second event indicated with #. The measured value at the thermocouple inside the reaction vessel but away from the susceptor (Outer Temp) continues to decrease as the heat transfer media is removed. When the turbopump is applied, there is a slight arrest in the Outer Temp thermocouple, indicating the completion of the removal of any residual gas media.

The desorption–recombination (DR) steps began with a temperature ramp from 760 °C to 800 °C (<1 min). The reaction vessel was isolated from the gas inlet and outlet, and a needle valve on a rotary vacuum pump was slowly opened to reduce the hydrogen pressure in the reaction vessel at a slow rate over 30 min. The rate was estimated by attempting to keep the measured temperature constant while the convection heating medium (the gas) was removed. During this process, two features are visible in the measured temperature data, corresponding to the completion of two separate desorption events. At the end of the 30 min, the vacuum pump needle valve was closed at approximately 500 mTorr, and a stronger vacuum was applied via a spun-up turbopump. The application of this vacuum and the removal of the remaining heat transfer media results in the third feature in our measured profile. This vacuum is applied for an additional 30 min, with a resulting pressure of approximately 10 mTorr. At this time, the induction coil current was turned off, and the sample was then allowed to furnace-cool in the vacuum environment until it reached room temperature.

The reaction vessel was then sealed off using the gate valve and placed in a helium-filled glovebox for further sample handling and storage. Portions of sample (notably still solid and sometimes cracked but essentially monolithic) were crushed in the helium glovebox and characterized via powder X-ray diffraction (PXRD) in air. Samples processed in a 2 T magnetic field were noticeably more difficult to handle, as the crushed powder was magnetized and attracted to itself. PXRD was performed with a PANalytical X’Pert Pro diffractometer (Panalytical, Worcestershire, UK) using a Cu K_{α} source, and the resulting data were analyzed via the HighScorePlus software package (v.4.8) [44].

Upon verification of $\text{Nd}_2\text{Fe}_{14}\text{B}$ phase formation, portions of the samples were crushed, and a small mass (~5 mg) was mixed in paraffin wax and measured in a Quantum Design MPMS XL SQUID magnetometer (Quantum Design, San Diego, CA, USA). Magnetometry measurements were performed by heating the sample and wax to above the wax melting point (~320 K) in zero applied magnetic field to suspend the sample in the wax, then by cooling to 300 K. The applied field was then raised to +5 T, and a hysteresis loop was

performed to -5 T and back to obtain the “unaligned” magnetization loop. To measure the magnetically aligned properties, while the magnetometer was at $+5$ T, the sample was again heated to 320 K to melt the wax and allow powder particles to reorient in response to the field. The wax was then solidified by cooling to 300 K, and an additional “aligned” magnetization loop was measured.

The magnetic data have been scaled utilizing two geometric demagnetization factors of 0.22 and 0.33 . The significance of the demagnetization factor can be seen through the equation:

$$H = H_{\text{appl}} - (N \times M) \quad (1)$$

where H is the scaled field, H_{appl} is the applied field, N is the demagnetization factor, and M is the powder magnetization. Determining N has been explored for several three-dimensional geometries [45–50], useful for single crystal measurements, but for a powder, it can be shown specifically for a sample of spherical particles that

$$N = \left(\frac{1}{3}\right) + f \left(D_z - \left(\frac{1}{3}\right)\right) \quad (2)$$

where D_z is the demagnetization factor due to the shape of the packing of the powder (NOT the particles within, which as stated are assumed to be spherical), and f is the packing fraction of the powder.

Bjork and Bahl discuss how the extremes of this equation may present themselves: A D_z of $1/3$ (as if the powder packing was spherical) would result in $N = 1/3$, as would a low packing density of the powder where the particulates do not interact magnetically [47]. The latter is unlikely to be the case with $\text{Nd}_2\text{Fe}_{14}\text{B}$ due to the material’s large internal magnetic field. Determination of the demagnetization factor of a powder sample is therefore difficult to ascertain experimentally, requiring both a controlled geometric packing of the powder into a specific shape, as well as reducing any geometric variance of the powder itself to “spheres”.

The packing shape of the powder is not strictly controlled in our characterization. Rather, it was found that a value of $D_z = 0.33$ produced non-physical magnetization curves in some samples. Treating this as an upward bound, we established that assuming a constant D_z , the values of N vary linearly with f . At this point, with an indeterminable value of f , the effect of both the minimum (0) and maximum (0.33) demagnetization factors may be considered reasonable bounds on the actual magnetic behavior of the sample. It becomes evident that so long as the hysteresis loop remains physical (that is, approaching a square-shaped loop as opposed to an “S” shaped loop, where the quadrant 2 and 4 behavior is non-functional), the larger demagnetization factor (up to 0.33) results in magnetic property values of greater magnitude than smaller values of N . Due to this, values are presented based on $N = 0.33$ when the behavior is physical, and in other cases is represented as $N = 0.22$ as a reasonable estimate of the true magnetization of the powder sample.

3. Results

3.1. Phase Characterization of Samples Processed with and without an Applied Field

In this work, both the HD and DR steps were performed either consistently without an applied field (notated as 0 T) or with an applied field of 2 Tesla (notated as 2 T). Diffraction patterns (See Figure 3) of the resultant samples show little to no consistent dependence on the application of a 2 T field. In both the 0 T and 2 T cases, the phases produced include primarily the $\text{Nd}_2\text{Fe}_{14}\text{B}$ phase, with minor inclusions of a cubic Nd oxide (previously cited as a grain boundary phase in sintered magnets, fcc-NdO_x) and Fe that either formed during the HD step but was left unreacted after the DR step or was present in excess in the original sample [51–59].

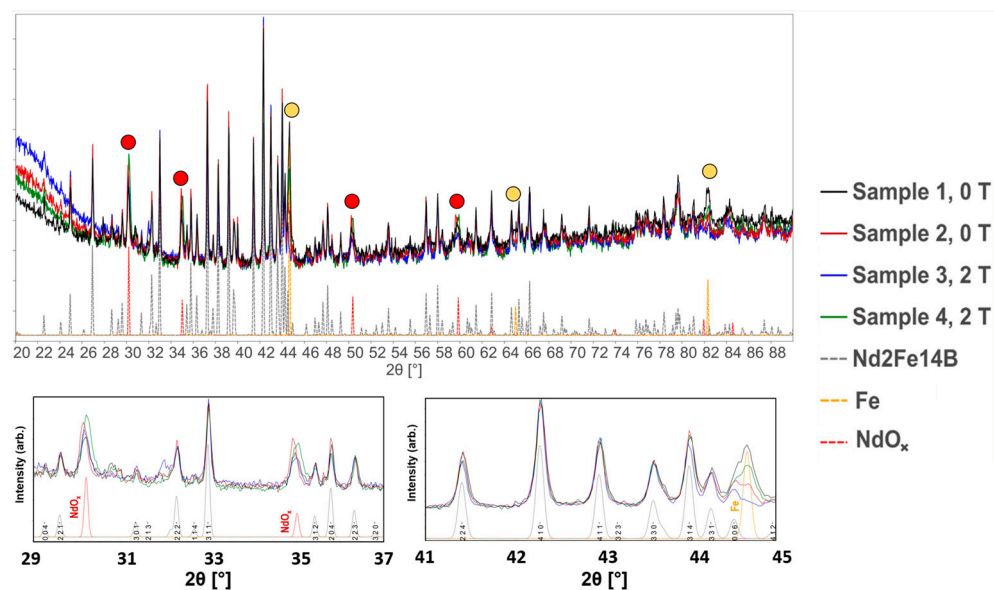


Figure 3. Ranges of 2θ indicate the presence of secondary phases in samples 1–4. hkl indices for the $\text{Nd}_2\text{Fe}_{14}\text{B}$ phases are labeled.

Of interest is the variable amount of the magnetically soft α -Fe phase in the resultant material regardless of the applied field. Previous work indicates that the presence of the applied field stabilizes the magnetically soft transition metal phases (below their magnetic T_C ; in this case, α -Fe has a $T_C = 770^\circ\text{C}$) during the DR step, such that DR needs to be performed at higher temperatures to reach the critical energy of reaction to re-form the parent compound [42,43]. In the case of our 2 T applied field, we find that 800°C provides enough heat to drive the reaction to completion regardless of the stabilizing effect of the 2 T applied field, as judged by the hydrogen desorption. Therefore, the presence of Fe in some samples post-HDDR is likely due to the formation of Nd-based oxides altering the stoichiometry prior to/during recombination. We expect this is due to the inhomogeneous feedstock due to the lack of correlation between the α -Fe and fcc- NdO_x wt.%, as seen in Table 2.

Table 2. Results from Rietveld refinement of powder X-ray diffraction data from samples 1–4.

#	Processing Field (T)	$\text{Nd}_2\text{Fe}_{14}\text{B}$ wt.%	$\text{Nd}_2\text{Fe}_{14}\text{B}$ R_{Bragg} %	α -Fe wt.%	α -Fe R_{Bragg} %	NdO_x wt.%	NdO_x R_{Bragg} %	Nd_2O_3 wt.%	Nd_2O_3 R_{Bragg} %	Nd_2O_3 wt.%	Nd_2O_3 R_{Bragg} %
1	0	77.0	3.04	13.2	1.28	6.5	1.24	1.6	1.93	1.7	2.00
2	0	88.7	2.45	4.5	0.55	6.8	2.20	-	-	-	-
3	2	93.9	4.75	0.7	0.75	5.4	2.35	-	-	-	-
4	2	82.0	3.74	8.7	0.445	9.3	2.43	-	-	-	-

Corresponding R_{wp} values for samples 1, 2, 3, and 4 are 3.55%, 3.47%, 4.54%, and 4.25%, respectively. $R_{\text{wp}} = \sqrt{\sum(w(Y_o - Y_c)^2 / \sum w(Y_o)^2)}$; $R_{\text{Bragg}} = \sum |I_o - I_c| / \sum I_o$, where Y_o and Y_c are the observed and calculated profile intensities, respectively, while I_o and I_c are the corresponding intensities of Bragg peaks of individual phases.

Rietveld refinement on the resulting patterns indicates that the phase fraction of fcc- NdO_x ranges from ~5.4 to 9.3 wt.% of the final product regardless of the applied magnetic field. Mo et al. found that the structure of Nd oxides in the grain boundary was dependent on the oxygen content in the sintered magnets, estimating that the oxygen content relative to Nd needed to fall between 9 at.% and 43 at.% [58]. Though the presence of this phase undoubtedly affects our resultant magnetic properties, we find that the coercivity values remain fairly consistent. This indicates a systematic inclusion of oxygen in our reaction; possible sources of contamination include a small leak in the experimental apparatus, small

enough that oxidation does not present itself in the reducing hydrogen atmosphere of HD but is still present in the material post-DR.

A particular goal of utilizing new processing methods for HDDR is establishing a higher level of microstructural control of grain sizes and crystal texture that approaches the single grain, single magnetic domain size (~300 nm) and a strong c-axis crystal texture. Success in this area would result in powders with higher coercivity, greater anisotropy, higher remanence, and consequently a higher energy product. In prior work, thermal processing of amorphous Nd-Fe-B under a magnetic field typically reduced the grain size of the product relative to the processes performed at ambient conditions [60].

We utilize Williamson–Hall plots to estimate the crystallite size produced from our dynamic-HDDR methodology in the four different samples [61]. The peak position in 2θ and full-width half-max (FWHM) of each peak were determined using the profile fitting procedure implemented in HighScorePlus. Instrumental broadening was determined using a lanthanum hexaboride standard to profile the U , V , and W peak parameters (for our instrument, U , V , and W are 0.0015, 0.002, and 0.0013, respectively). For each peak position, these parameters can determine the angle-dependent instrumental broadening β_{Inst} via the following equation:

$$\beta_{Inst} = \sqrt{U \cdot \tan^2(\theta) + V \cdot \tan(\theta) + W} \quad (3)$$

For each peak, the intrinsic FWHM (hereafter referred to as β_{tot}) can be determined with the difference between the measured FWHM and the β_{Inst} . In our case, all peaks determined with our Rietveld fit to correspond to the Nd₂Fe₁₄B phase were included in our plot. The Williamson–Hall method deconvolutes peak broadening effects of crystallite size (β_L) and strain (β_e) and represents them in terms of their angle dependence using the following two equations:

$$\beta_L = \frac{K\lambda}{L \cdot \cos(\theta)} \quad (4)$$

$$\beta_e = C\varepsilon \cdot \tan(\theta) \quad (5)$$

where K is a constant between 0.9 and 1, λ is the wavelength of the characterizing X-rays, L is the crystallite size, and C is a constant modifier to the ε (strain) often falling between 4 and 5. If the convolution of the two is assumed to be additive, the combined broadening effect is $\beta_{tot} = \beta_L + \beta_e$. If both sides of this equivalency are multiplied by the value of $\cos(\theta)$, the result is the following equation:

$$\beta_{tot} \cos(\theta) = C\varepsilon \cdot \sin(\theta) + \frac{K\lambda}{L} \quad (6)$$

which can be plotted as a relationship between $\beta_{tot} \times \cos(\theta)$ and $\sin(\theta)$. The result of a linear fit of this relationship ($y = mx + b$) will have a y-intercept equivalent to $(K\lambda/L)$ and a slope equivalent to $C\varepsilon$ (see Figure 4). The crystallite size L found using the y-intercept of the linear fit therefore represents the crystallite size while accounting for the strain. In comparison, calculating L values for individual peaks and finding the mean gives an average L value with an assumed strain of zero at every analyzed peak. As shown in Table 3, the deviation of this “average” crystallite size diameter is nearly encompassed by those values found with the Williamson–Hall method, suggesting that the small values of strain do little to alter the expected crystallite sizes.

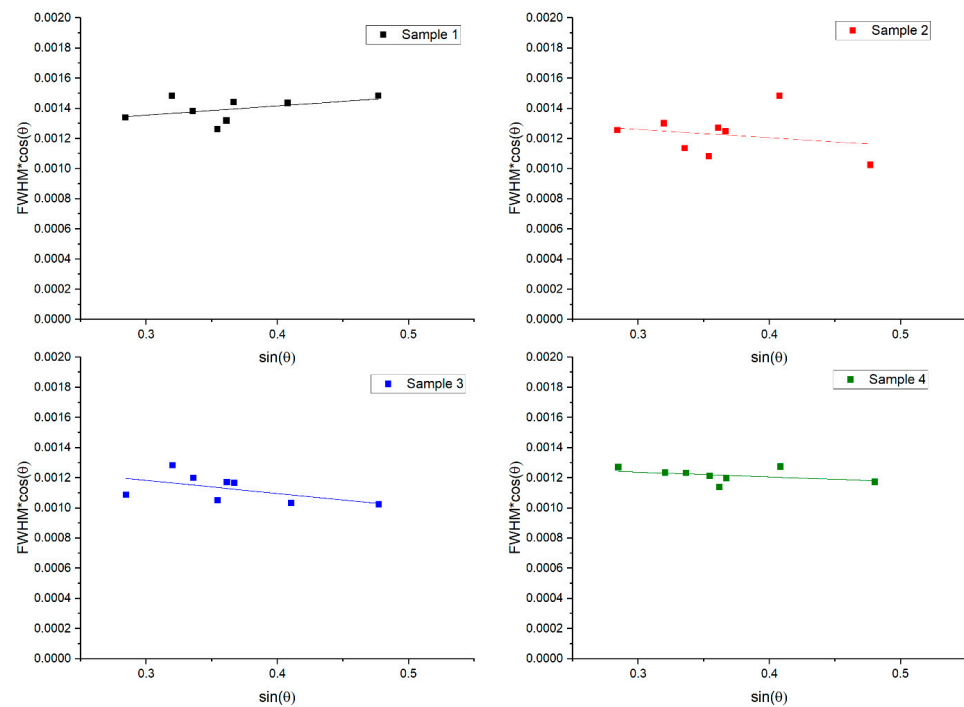


Figure 4. Williamson–Hall plots including linear fits with sample 1 in black, sample 2 in red, sample 3 in blue, and sample 4 in green. Parameters are shown in Table 3.

Table 3. Relevant Williamson–Hall fit parameters and resultant values of samples 1–4.

#	Processing Field (T)	Slope ($C\epsilon$)	Y-Intercept ($K\lambda/L$)	Williamson–Hall Diameter (L , nm)	Strain ($ C\epsilon $, $\text{\AA}/\text{\AA}$)	Average Crystallite Diameter (L_{avg} , nm)
1	0	0.0006 (5)	0.0012 (2)	121 (1)	0.0006 (5)	102 (6)
2	0	−0.0005 (10)	0.0014 (4)	99 (5)	0.0005 (10)	117 (14)
3	2	−0.0009 (5)	0.0014 (2)	98 (2)	0.0009 (5)	126 (10)
4	2	−0.0003 (3)	0.0013 (1)	106 (1)	0.0003 (3)	117 (5)

Uncertainties do not represent the assumptions made in the Williamson–Hall method.

In this method, it is more informative to have well-resolved peaks in a wider range of 2θ . However, three primary factors limit the peaks chosen in our analysis: the secondary phases present, air scattering at low 2θ , and peak overlap (low resolution) at high 2θ values. Well-resolved peaks were chosen from among the remainder and held consistent for each sample, with hkl indices of in order of increasing 2θ value.

Further, we compared the 0 T and 2 T samples to determine whether the application of a magnetic field has a reliable effect on the resulting crystallite size (Figure 5). We found that in most of our samples, our minimum grain size falls within the range of 95–125 nm, suggesting our processing method results in particle sizes smaller than a single magnetic domain regardless of the applied field. Additionally, the field did not result in grain sizes outside the range of sizes seen in the samples processed at an ambient field when characterized using this method. It is important to note that although the Williamson–Hall method provides a value for the crystallite diameter, if the sample itself has a range of sizes, that information will be lost. Additionally, magnetic characteristics can be affected by non-uniform grain sizes and shapes, and prior literature suggests that the “dynamic” HDDR method may be responsible for a wider range of crystallite sizes [21]. Therefore, characterization of the sample utilizing scanning electron microscopy techniques is necessary and ongoing.

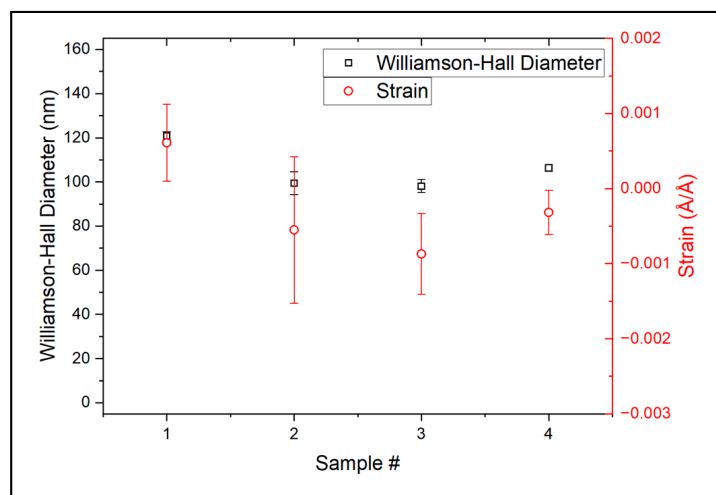


Figure 5. The Williamson–Hall average crystallite diameter and strain resulting from the Williamson–Hall analysis of each sample 1–4. Error bars may be smaller than the data point.

This leaves room for additional optimization of the heating profile and other processing parameters toward an ideal average microstructural grain size. Work is ongoing to determine whether the application of a magnetic field results in 1. a different ideal hydrogen percentage in the supply gas and/or 2. a change in dwell times to re-optimize the microstructural and magnetic character of the resulting samples.

3.2. Magnetization of Samples Processed with and without an Applied Field

The presence or absence of an applied magnetic field during our HDDR process had minor consequences on the ultimate phase formation and average grain size. However, the field has a greater effect on the magnetic properties of the resultant material, indicating a degree of microstructural dependence. Samples processed at 0 T and 2 T had differences between the saturation magnetization of the aligned and unaligned loops, indicating our HDDR heating profile and reaction apparatus maintained some of the local crystallographic alignment of grains in the starting material (Table 4).

Table 4. Relevant magnetic property values of samples 1–4.

#	Processing Field (T)	Demagnetization Factor	Alignment	Magnetization at 5 T, $M_{@5T}$ (emu/g)	Remanence, M_R (emu/g)	$M_R/M_{@5T}$	Coercivity, H_{ci} (kOe)	Maximum Energy Product, $(BH)_{max}$ (MG \times Oe)
1	0	0.33	Unaligned	122	62	-	2.5	-
			Aligned	125	79	0.63		7.0
2	0	0.22	Unaligned	149	72	-	3.4	-
			Aligned	155	104	0.67		10.5
3	2	0.22	Unaligned	137	79	-	2.3	-
			Aligned	139	102	0.73		8.7
4	2	0.33	Unaligned	145	87	-	2	-
			Aligned	148	104	0.70		8.6

In much of the literature, the hydrogen partial pressure is given as the processing parameter, and the total pressure of the supplied gas may not be formally addressed. $M_R/M_{@5T}$ is provided only for the aligned samples.

The application of a 2 T magnetic field during HDDR processing resulted in a material with greater remanence and magnetic saturation but a lower coercivity than that of the 0 T sample. However, we observe that the application of the 2 T magnetic field during processing also enhances the magnetic anisotropy of the sample. This is difficult to quantify

with the “degree of alignment” (*DOA*) metric, but it is apparent in the “ratio of remanence to saturation” (M_R/M_{sat}) metric.

The *DOA* metric is a comparison of the magnetic response of the powder when it is unaligned or randomized compared to when it is ordered through magnetic alignment. One way to quantify this using magnetization data is [18,62]

$$D.O.A. = 2 \left(M_{R,aligned} - M_{R,unaligned} \right) / \left(M_{R,aligned} \right) \quad (7)$$

This metric is useful for traditionally processed samples, as well as for our samples processed at 0 T. However, the application of the 2 T processing magnetic field and the resulting magnetization of the product causes the $M_{R,unaligned}$ value to be misrepresented in this equation, as the unaligned magnetic remanence will not represent a true randomness of orientation of the powder. Heating the magnetized powder above its Curie temperature would remove this complication, but care must be taken to perform this additional step in an oxygen-free environment. Without this step, we would expect the value of the *DOA* for the 2 T sample to underestimate this quantity to a varying degree based on sample selection.

An additional way to compare the magnetic anisotropy of the polycrystalline system is the value of the M_R/M_{sat} ratio. When quantified for the “aligned” magnetization loops, this quantity indicates how the alignment of particles along their easy magnetization axis (while directionally stabilized by the applied magnetic field, represented by M_{sat}) causes the material to retain its magnetization as the applied field is reduced to zero (represented by M_R). The ratio of the two indicates how well the material aligns along the optimal easy axis without the stabilizing effect of the field; a value of unity would indicate the material does not need to interact with the external field to remain aligned.

For randomly oriented non-interacting particles, $M_R/M_{sat} = 0.5$. Any alignment along the measurement direction will increase this value up to a theoretical maximum of 1 [63]. In our case, our maximum applied field is $H = 5$ T for all samples consistently, and the M_{sat} value in this ratio is replaced with the $M_{@5T}$ value. However, if the measurement was performed with higher applied fields, the magnetization may slightly increase, reducing the absolute value of the ratio. The use of $M_{@5T}$ in this ratio may result in inflated ratios but is useful to compare in a consistent way across samples.

In the case of the aligned loop of the 0 T processed sample, the $M_R/M_{@5T}$ ratio value ranges from 0.63–0.66, while the ratio in the 2 T aligned loop ranges from 0.70–0.73. This comparison is more easily observed when the M vs. H loops are normalized to their $M_{@5T}$ value, as shown in Figure 6. Using this metric, the application of the field during HD and DR processing notably enhances the anisotropy of the resulting material.

The repeatable increase in the M_R/M_{sat} caused by the external magnetic field does not increase the magnetic property values of the resultant Nd-Fe-B powder to the cutting edge of the literature. This is for several reasons: the ternary composition of our alloy is not optimized, and no additional grain boundary additive is included. Further, the HDDR methodology is often investigated as a part of studies, and processing parameters are often dissimilar. Finally, studies regarding applied magnetic field HDDR processing are uncommon, with very few examples available. However, our HDDR process is very similar to Liu et al. [18]. When comparing our run at 0 T to their analogous no-field run, the M_R/M_{sat} values found (when M_{sat} is measured at 3 T, the extent of the referenced data) are 0.72 and 0.80, respectively. Although this somewhat indicates a deterioration in performance, that deterioration may be caused by variables such as our different apparatus, our applied demagnetization factor, or our NdO_x concentration, just to name a few possibilities.

It is worth noting in these plots that the squareness of these loops is not necessarily indicative of a high-performance powder; rather, the application of the aforementioned demagnetization correction as applied to a powder sample is at least partially responsible. However, although the application of a demagnetization factor has become common, it is worth noting that the form of the correction we use is a modification of an equation

originally intended for single crystalline samples. The broad generalization of reducing geometric factors of multi-sized and -shaped particles to the packing fraction and packing shape is almost assuredly missing relevant information, and the characterization of permanent magnet powders would benefit significantly from future standardization.

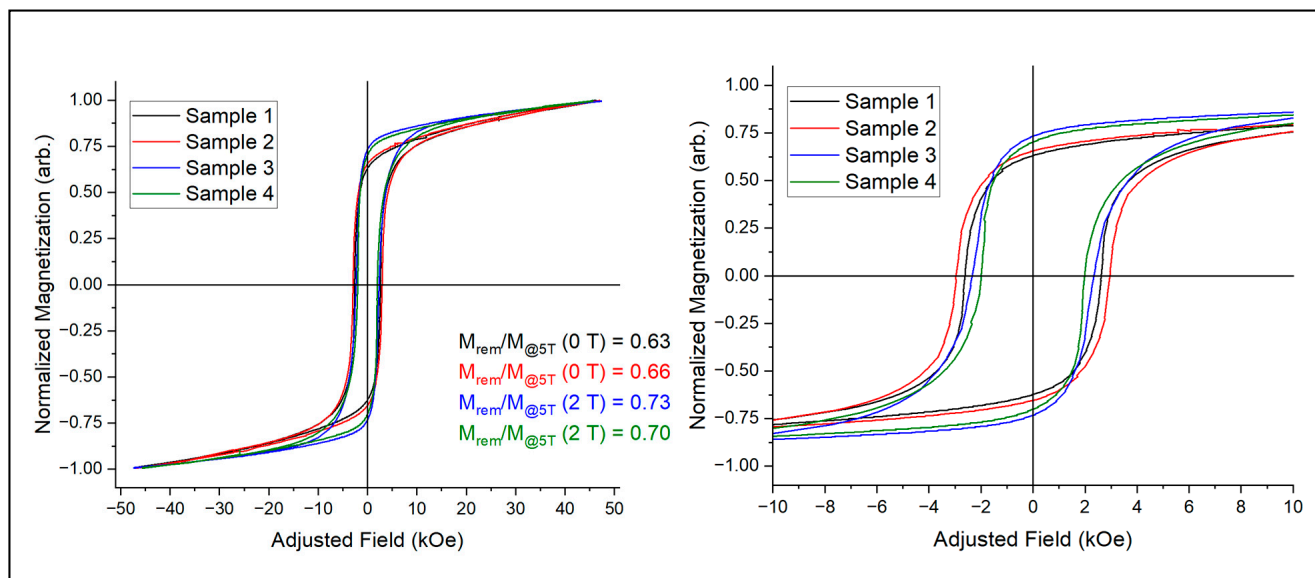


Figure 6. The aligned M vs. H curves normalized to the samples' $M_{@5T}$ values show a distinct difference in how samples processed in the field maintain their magnetization as the applied field is removed. The full range of applied field measured is shown on the left, with a reduced range shown on the right. The x-axis is labeled “adjusted” to represent the application of a demagnetization factor.

4. Conclusions

Our ongoing work to produce anisotropic powder through a dynamic-HDDR process with simultaneous magnetic field has resulted in a repeatable increase in magnetic anisotropy of the resultant samples. As our work continues, the changes wrought by the applied field reveal multiple avenues for optimization of the thermal and hydrogen parameters of our process, including a more homogenous feedstock, an exploration of HD and DR dwell temperatures under a magnetic field, and a tighter control of the desorption vacuum step. As the phase content of the powder and grain size are optimized, the coercivity, remanence, and resulting energy product stand to make significant strides due to the increased anisotropy.

Author Contributions: Conceptualizations, M.A.M. and M.S.K.; Methodology, M.A.M. and M.S.K.; Formal Analysis, Z.P.T.; Investigation, Z.P.T., X.L., M.A.M. and M.S.K.; Resources, X.L., I.C.N., M.A.M. and M.S.K.; Writing—original draft preparations, Z.P.T.; Writing—review and editing, X.L., I.C.N., M.J.K., M.A.M. and M.S.K.; Visualization, Z.P.T.; Supervision, M.S.K.; Project Administration, I.C.N. and M.S.K.; Funding acquisition, M.S.K. All authors have read and agreed to the published version of the manuscript.

Funding: This work is supported by the Critical Materials Institute, an Energy Innovation Hub funded by the U.S. Department of Energy, Office of Energy Efficiency and Renewable Energy, Advanced Manufacturing Office, under DOE Contract DE-AC02-07CH11358.

Data Availability Statement: The data presented in this study are available on request from the corresponding author (legal).

Conflicts of Interest: The authors declare that they have no known competing financial interests or personal relationships that could have appeared to influence the work reported in this paper.

References

1. Cui, J.; Ormerod, J.; Parker, D.; Ott, R.; Palasyuk, A.; McCall, S.; Paranthaman, M.P.; Kesler, M.S.; McGuire, M.A.; Nlebedim, I.C.; et al. Manufacturing Processes for Permanent Magnets: Part I—Sintering and Casting. *JOM* **2022**, *74*, 1279–1295. [[CrossRef](#)]
2. Cui, J.; Ormerod, J.; Parker, D.S.; Ott, R.; Palasyuk, A.; McCall, S.; Paranthaman, M.P.; Kesler, M.S.; McGuire, M.A.; Nlebedim, C.; et al. Manufacturing Processes for Permanent Magnets: Part II—Bonding and Emerging Methods. *JOM* **2022**, *74*, 2492–2506. [[CrossRef](#)]
3. Kramer, M.J.; McCallum, R.W.; Anderson, I.A.; Constantinides, S. Prospects for Non-Rare Earth Permanent Magnets for Traction Motors and Generators. *JOM* **2012**, *64*, 752–763. [[CrossRef](#)]
4. Takeshita, T.; Nakayama, R. Magnetic Property and Microstructure of NdFeB Magnet Powder Produced by Hydrogen Treatment. In Proceedings of the 10th International Workshop on Rare-Earth Magnets and Their Applications, Kyoto, Japan, 16–19 May 1989; pp. 551–558.
5. Nakayama, R.; Takeshita, T.; Itakura, M.; Kuwano, N.; Oki, K. Magnetic properties and microstructures of the Nd-Fe-B magnet powder produced by hydrogen treatment. *J. Appl. Phys.* **1991**, *70*, 3770–3774. [[CrossRef](#)]
6. Harris, I.R.; McGuinness, P.J. Hydrogen: Its use in the processing of NdFeB-type magnets. *J. Less Common Met.* **1991**, *172–174*, 1273–1284. [[CrossRef](#)]
7. Elton, J.; Oesterreicher, H. Hydriding system for moderately severe conditions of pressure and temperatures. *Rev. Sci. Instrum.* **1983**, *54*, 1684–1686. [[CrossRef](#)]
8. Higgins, B.; Oesterreicher, H. Properties and stability of Nd₂Fe₁₄B particles. *IEEE Trans. Magn.* **1987**, *23*, 92–93. [[CrossRef](#)]
9. Harris, I.R. The potential of hydrogen in permanent magnet production. *J. Less Common Met.* **1987**, *131*, 245–262. [[CrossRef](#)]
10. Ragg, O. The HD and HDDR processes in the production of Nd-Fe-B permanent magnets. *Int. J. Hydrogen Energy* **1997**, *22*, 333–342. [[CrossRef](#)]
11. Nakamura, H.; Kato, K.; Book, D.; Sugimoto, S.; Okada, M.; Homma, M. Enhancement of coercivity in high remanence HDDR Nd-Fe-B powders. *IEEE Trans. Magn.* **1999**, *35*, 3274–3276. [[CrossRef](#)]
12. Gutfleisch, O.; Short, C.; Verdier, M.; Harris, I.R. The effect of hydrogen pressure on the kinetics of the HDDR-process of bulk Nd-Fe-B-type alloys. *IEEE Trans. Magn.* **1994**, *30*, 642–644. [[CrossRef](#)]
13. Gutfleisch, O.; Khlopkov, K.; Teresiak, A.; Muller, K.H.; Drazic, G.; Mishima, C.; Honkura, Y. Memory of texture during HDDR processing of NdFeB. *IEEE Trans. Magn.* **2003**, *39*, 2926–2931. [[CrossRef](#)]
14. Gutfleisch, O.; Güth, K.; Woodcock, T.G.; Schultz, L. Recycling Used Nd-Fe-B Sintered Magnets via a Hydrogen-Based Route to Produce Anisotropic, Resin Bonded Magnets. *Adv. Energy Mater.* **2012**, *3*, 151–155. [[CrossRef](#)]
15. Sepehri-Amin, H.; Ohkubo, T.; Hono, K.; Güth, K.; Gutfleisch, O. Mechanism of the texture development in hydrogen-disproportionation-desorption-recombination (HDDR) processed Nd-Fe-B powders. *Acta Mater.* **2015**, *85*, 42–52. [[CrossRef](#)]
16. Horikawa, T.; Matsuura, M.; Sugimoto, S.; Yamazaki, M.; Mishima, C. Crystallographic alignment in the recombination stage in d-HDDR process of Nd-Fe-B-Ga-Nb powders. *AIP Adv.* **2016**, *6*, 056017. [[CrossRef](#)]
17. Horikawa, T.; Yamazaki, M.; Mishima, C.; Matsuura, M.; Sugimoto, S. Magnetic anisotropy and crystallographic alignment in Fe and NdH₂ during d-HDDR process of Nd-Fe-B-Ga-Nb powders. *AIP Adv.* **2019**, *9*, 035244. [[CrossRef](#)]
18. Liu, X.B.; Kesler, M.S.; Besser, M.F.; Kramer, M.J.; McGuire, M.A.; Nlebedim, I.C. Effect of Processing Hydrogen Pressure on Magnetic Properties of HDDR Nd-Fe-B Magnet. *IEEE Trans. Magn.* **2021**, *57*, 2100604. [[CrossRef](#)]
19. McGuinness, P.J.; Short, C.L.; Harris, I.R. Anisotropic HDDR epoxy bonded magnets from NdFeBZr. *IEEE Trans. Magn.* **1992**, *28*, 2160–2162. [[CrossRef](#)]
20. Liesert, S.; Fruchart, D.; de Rango, P.; Soubeyroux, J.L. The hydrogenation-disproportionation-desorption-recombination process of Nd₂Fe₁₄B studied by in-situ neutron diffraction and thermomagnetic measurements. *J. Alloys Compd.* **1997**, *253–254*, 140–143. [[CrossRef](#)]
21. Engerhoff, J.A.B.; Keller, F.O.; Lopes, L.U.; Mascheroni, A.A.; Takiishi, H.; Wendhausen, P.A.P. d-HDDR Processing of Nd-Fe-B Based Alloys to Obtain Highly Anisotropic Nanocrystalline Powders. *Mater. Sci. Forum* **2017**, *899*, 563–566. [[CrossRef](#)]
22. Sugimoto, S.; Nakamura, H.; Kato, K.; Book, D.; Kagotani, T.; Okada, M.; Homma, M. Effect of the disproportionation and recombination stages of the HDDR process on the inducement of anisotropy in Nd-Fe-B magnets. *J. Alloys Compd.* **1999**, *293–295*, 862–867. [[CrossRef](#)]
23. Sugimoto, S.; Book, D. HDDR Process for the Production of High Performance Rare-Earth Magnets. In *Handbook of Advanced Magnetic Materials*; Liu, Y., Sellmyer, D.J., Shindo, D., Eds.; Springer: Boston, MA, USA, 2006.
24. Tomida, T.; Choi, P.; Maehara, Y.; Uehara, M.; Tomizawa, H.; Hirose, S. Origin of magnetic anisotropy formation in the HDDR-process of Nd₂Fe₁₄B-based alloys. *J. Alloys Compd.* **1996**, *242*, 129–135. [[CrossRef](#)]
25. Gutfleisch, O.; Harris, I.R. Fundamental and practical aspects of the hydrogenation, disproportionation, desorption and recombination process. *J. Phys. D Appl. Phys.* **1996**, *29*, 2255–2265. [[CrossRef](#)]
26. Gutfleisch, O.; Matzinger, M.; Fidler, J.; Harris, I.R. Characterisation of solid-HDDR processed Nd₁₆Fe₇₆B₈ alloys by means of electron microscopy. *J. Magn. Magn. Mater.* **1995**, *147*, 320–330. [[CrossRef](#)]
27. Yamazaki, M.; Horikawa, T.; Mishima, C.; Matsuura, M.; Tezuka, N.; Sugimoto, S. Effect of hydrogenation disproportionation conditions on magnetic anisotropy in Nd-Fe-B powder prepared by dynamic hydrogenation disproportionation desorption recombination. *AIP Adv.* **2017**, *7*, 056220. [[CrossRef](#)]

28. Gao, J.-R.; Song, X.-P.; Wang, X.-T. Effects of reduced hydrogen pressure on magnetic properties of HDDR-treated NdFeGaB alloy powders. *J. Alloys Compd.* **1998**, *267*, 270–273. [[CrossRef](#)]
29. Sugimoto, S.; Koike, N.; Book, D.; Kagotani, T.; Okada, M.; Inomata, K.; Homma, M. An improved HDDR treatment for the production of anisotropic Nd–Fe–B ternary powders. *J. Alloys Compd.* **2002**, *330–332*, 892–896. [[CrossRef](#)]
30. Nakamura, H.; Suefuji, R.; Sugimoto, S.; Okada, M.; Homma, M. Effects of HDDR treatment conditions on magnetic properties of Nd–Fe–B anisotropic powders. *J. Appl. Phys.* **1994**, *76*, 6828–6830. [[CrossRef](#)]
31. Liesert, S.; Kirchner, A.; Grünberger, W.; Handstein, A.; De Rango, P.; Fruchart, D.; Schultz, L.; Müller, K.H. Preparation of anisotropic NdFeB magnets with different Nd contents by hot deformation (die-upsetting) using hot-pressed HDDR powders. *J. Alloys Compd.* **1998**, *266*, 260–265. [[CrossRef](#)]
32. Liesert, S.; Fruchart, D.; de Rango, P.; Rivoirard, S.; Soubeyroux, J.L.; Perrier de la Bâthie, R.; Tournier, R. HDDR process of Nd–Fe–B with an excess of intergranular Nd-rich phase under magnetic field. *J. Alloys Compd.* **1997**, *262–263*, 366–371. [[CrossRef](#)]
33. Morimoto, K.; Katayama, N.; Akamine, H.; Itakura, M. Coercivity enhancement of anisotropic Dy-free Nd–Fe–B powders by conventional HDDR process. *J. Magn. Magn. Mater.* **2012**, *324*, 3723–3726. [[CrossRef](#)]
34. Takeshita, T.; Morimoto, K. Anisotropic Nd–Fe–B bonded magnets made from HDDR powders (invited). *J. Appl. Phys.* **1996**, *79*, 5040–5044. [[CrossRef](#)]
35. Uehara, M.; Tomizawa, H.; Hirosawa, S.; Tomida, T.; Maehara, Y. Origin of anisotropy in the HDDR process of Nd₂Fe₁₄B-based alloys. *IEEE Trans. Magn.* **1993**, *29*, 2770–2772. [[CrossRef](#)]
36. Liesert, S.; de Rango, P.; Soubeyroux, J.L.; Fruchart, D.; Perrier de la Bâthie, R. Anisotropic and coercive HDDR Nd–Fe–B powders prepared under magnetic field. *J. Magn. Magn. Mater.* **1996**, *157–158*, 57–58. [[CrossRef](#)]
37. Courtois, P.; Perrier de la Bâthie, R.; Tournier, R. Exploration of the magnetic field effect on the orientation of Nd₂Fe₁₄B crystallites at high temperatures. *J. Magn. Magn. Mater.* **1996**, *153*, 224–230. [[CrossRef](#)]
38. Rivoirard, S.; Barthem, V.M.T.S.; Bres, R.; Beaugnon, E.; de Miranda, P.E.V.; Givord, D. Texturing Nd–Fe–B magnets under high magnetic field. *J. Appl. Phys.* **2008**, *104*, 043915. [[CrossRef](#)]
39. de Rango, P.; Rivoirard, S.; Traverse, A.; Fruchart, D.; Genin, F.N. Role of Zr and Ga additions on the hydrogen process of Nd–Fe–B magnets. *J. Alloys Compd.* **2003**, *356–357*, 579–583. [[CrossRef](#)]
40. Luo, J. Development of Anisotropic Nd–Fe–B Powders from Sintered Magnets by Hydrogen Decrepitation/Desorption Process. Ph.D. Thesis, Universite Joseph-Fourier, Grenoble, France, 2009.
41. Luo, J.; De Rango, P.; Fruchart, D.; Mei, J.; Hu, R.; Li, J.; Zhou, L. Enhancing magnetic properties of anisotropic NdDyFeCoNbCuB powder by applying magnetic field at high temperature during hydrogen desorption. *Rare Met.* **2010**, *29*, 480–485. [[CrossRef](#)]
42. Rivoirard, S.; Lyubina, J.; Beaugnon, E.; Gutfeisch, O. Magnetic field effect on the hydrogen desorption and recombination reaction in disproportionated Sm–Co-type alloys. *Appl. Phys. Lett.* **2008**, *93*, 172509. [[CrossRef](#)]
43. Rivoirard, S. High Steady Magnetic Field Processing of Functional Magnetic Materials. *JOM* **2013**, *65*, 901–909. [[CrossRef](#)]
44. Degan, T.; Sadki, M.; Bron, E.; Konig, U.; Nenert, G. The HighScore Suite. *Powder Diffr.* **2014**, *29*, S13–S18. [[CrossRef](#)]
45. Aharoni, A. Demagnetizing factors for rectangular ferromagnetic prisms. *J. Appl. Phys.* **1998**, *83*, 3432–3434. [[CrossRef](#)]
46. Bahl, C.R.H. Estimating the demagnetization factors for regular permanent magnet pieces. *AIP Adv.* **2021**, *11*, 075028. [[CrossRef](#)]
47. Bjørk, R.; Bahl, C.R.H. Demagnetization factor for a powder of randomly packed spherical particles. *Appl. Phys. Lett.* **2013**, *103*, 102403. [[CrossRef](#)]
48. Bleaney, B.; Hull, R.A. The effective susceptibility of a paramagnetic powder. *Proc. R. Soc. Lond. Ser. A Math. Phys. Sci.* **1997**, *178*, 86–92. [[CrossRef](#)]
49. Breit, G. Calculations of the Effective Permeability and Dielectric Constant of a Powder. *Proc. R. Acad. Amst.* **1922**, *25*, 293–308.
50. Osborn, J.A. Demagnetizing Factors of the General Ellipsoid. *Phys. Rev.* **1945**, *67*, 351–357. [[CrossRef](#)]
51. Mazilkin, A.; Straumal, B.B.; Protasova, S.G.; Gorji, S.; Straumal, A.B.; Katter, M.; Schütz, G.; Barezky, B. Grain boundary oxide layers in NdFeB-based permanent magnets. *Mater. Des.* **2021**, *199*, 109417. [[CrossRef](#)]
52. Sasaki, T.T.; Ohkubo, T.; Hono, K. Structure and chemical compositions of the grain boundary phase in Nd–Fe–B sintered magnets. *Acta Mater.* **2016**, *115*, 269–277. [[CrossRef](#)]
53. Sasaki, T.T.; Ohkubo, T.; Takada, Y.; Sato, T.; Kato, A.; Kaneko, Y.; Hono, K. Formation of non-ferromagnetic grain boundary phase in a Ga-doped Nd-rich Nd–Fe–B sintered magnet. *Scr. Mater.* **2016**, *113*, 218–221. [[CrossRef](#)]
54. Kim, T.-H.; Lee, S.-R.; Namkung, S.; Jang, T.-S. A study on the Nd-rich phase evolution in the Nd–Fe–B sintered magnet and its mechanism during post-sintering annealing. *J. Alloys Compd.* **2012**, *537*, 261–268. [[CrossRef](#)]
55. Okazaki, H.; Billington, D.; Tsuji, N.; Ueno, W.; Kotani, Y.; Kawaguchi, S.; Sugimoto, K.; Toyoki, K.; Fukagawa, T.; Nishiuchi, T.; et al. Quantitative identification of constituent phases in a Nd–Fe–B–Cu sintered magnet and temperature dependent change of electron density of Nd₂Fe₁₄B studied by synchrotron X-ray diffraction. *Acta Mater.* **2019**, *181*, 530–536. [[CrossRef](#)]
56. Kobayashi, S.; Martín-Cid, A.; Toyoki, K.; Okazaki, H.; Hirosawa, S.; Nakamura, T. Influence of magnetostriction on the lattice constants of the secondary phases in Nd–Fe–B sintered magnets studied by synchrotron X-ray diffraction. *AIP Adv.* **2019**, *9*, 125154. [[CrossRef](#)]
57. Tsuji, N.; Okazaki, H.; Ueno, W.; Kotani, Y.; Billington, D.; Yasui, A.; Kawaguchi, S.; Sugimoto, K.; Toyoki, K.; Fukagawa, T.; et al. Temperature dependence of the crystal structures and phase fractions of secondary phases in a Nd–Fe–B sintered magnet. *Acta Mater.* **2018**, *154*, 25–32. [[CrossRef](#)]

58. Mo, W.; Zhang, L.; Liu, Q.; Shan, A.; Wu, J.; Komuro, M. Dependence of the crystal structure of the Nd-rich phase on oxygen content in an Nd–Fe–B sintered magnet. *Scr. Mater.* **2008**, *59*, 179–182. [[CrossRef](#)]
59. Fidler, J. On the role of the ND-rich phases in sintered ND-Fe-B magnets. *IEEE Trans. Magn.* **1987**, *23*, 2106–2108. [[CrossRef](#)]
60. Kesler, M.; Jensen, B.; Zhou, L.; Palasyuk, O.; Kim, T.-H.; Kramer, M.; Nlebedim, I.; Rios, O.; McGuire, M. Effects of High Magnetic Fields on Phase Transformations in Amorphous Nd₂Fe₁₄B. *Magnetochemistry* **2019**, *5*, 16. [[CrossRef](#)]
61. Williamson, G.K.; Hall, W.H. X-ray line broadening from filed aluminium and wolfram. *Acta Metall.* **1953**, *1*, 22–31. [[CrossRef](#)]
62. Zhai, F.; Sun, A.; Yuan, D.; Wang, J.; Wu, S.; Volinsky, A.A.; Wang, Z. Epoxy resin effect on anisotropic Nd–Fe–B rubber-bonded magnets performance. *J. Alloys Compd.* **2011**, *509*, 687–690. [[CrossRef](#)]
63. Coey, J.M.D. *Magnetism and Magnetic Materials*; Cambridge University Press: Cambridge, UK, 2010. [[CrossRef](#)]

Disclaimer/Publisher’s Note: The statements, opinions and data contained in all publications are solely those of the individual author(s) and contributor(s) and not of MDPI and/or the editor(s). MDPI and/or the editor(s) disclaim responsibility for any injury to people or property resulting from any ideas, methods, instructions or products referred to in the content.